JOURNAL OF MATERIALS SCIENCE 25 (1990) 2118–2124

Characterization of nanoporosity in polymer-derived ceramic fibres by X-ray scattering techniques

JONATHAN LIPOWITZ, JAMES A. RABE, LUDO K. FREVEL
Dow Corning Corporation, Midland, Michigan 48686, USA

ROBERT L. MILLER
Michigan Molecular Institute, Midland, Michigan 48640, USA

Ceramic fibres with Si–C–O and Si–N–C–O compositions, prepared by pyrolysis of polymer precursors, generally have densities lower than those calculated from a volume additivity rule. However, techniques often used to detect porosity such as electron microscopy methods, surface area and porosimetry measurements show that little surface-connected porosity is present. X-ray scattering measurements, both wide-angle (WAXS) and small-angle (SAXS), show considerable scattering in the range $1^\circ < 2\theta < 10^\circ$ (Cu$K\alpha$). Treatment of the scattering data by the classical Guinier (low angle limit) and Porod (high angle limit) methods indicate that closed, globular, nanometre-scale porosity (1 to 3 nm diameter) is present in all ceramic fibres examined. X-ray scattering power correlates quantitatively with the volume fraction porosity, as expected if porosity is the dominant factor affecting X-ray scattering. Nanoparticles of excess carbon and of β-SiC nanocrystallites, though present, are minor contributors to the scattering of X-rays in these ceramic fibres. Fibres are three-dimensional, not of fractal dimension, and are not oriented. As density increases with increasing pyrolysis temperature, average pore size increases and pore volume fraction decreases. This results from a thermodynamically favourable reduction of surface free energy and apparently occurs by a viscous flow process.

1. Introduction

There has been much recent interest in the preparation of ceramic materials, especially fibres, by pyrolysis of shaped, thermoplastic polymer precursors [1–6]. Silicon-based ceramic fibres produced in these processes at the usual pyrolysis temperature of 1000 to 1400° C are largely amorphous [7]. The structure of the continuous amorphous phase can be considered as a three-dimensional random cross linking of Si(C, N, O)$_4$ tetrahedra, forming silicon oxycarbonitrides or silicon oxycarbides. Embedded in this amorphous phase are excess carbon nanoparticles similar to the pyrolytic carbons, having a well-developed two-dimensional turbostratic structure. In the Si–C–O ceramics a nanocrystalline β-SiC phase is also present.

Calculations using a rule of mixtures based on volume additivities for components in their appropriate states (amorphous or crystalline) [7] indicate that all these ceramic fibres are lower in density than theoretical (Equation 1), implying the presence of voids (up to 25%):

$$\varrho_t = \sum_i V_i \varrho_i \qquad (1)$$

where ϱ_t = theoretical density, V_i = volume fraction of phase i and ϱ_i = density of phase i. However, a variety of measurements used to detect surface-connected porosity such as BET surface area and mercury porosimetry [8] indicated that surface areas are close to geometric for the fibres in question. That is, little or no open porosity is present. Various methods able to detect porosity such as SEM and TEM techniques as well as BET surface area and mercury porosimetry measurements on powdered ceramic fibres failed to detect more than small amounts of porosity (1 to 3%).

X-ray scattering techniques have been widely used to characterize inhomogeneities in electron density, including void volume in materials [9, 10]. This paper describes X-ray scattering measurements on a variety of ceramic fibres in an attempt to characterize the void volume in these fibres. In addition, an understanding of the origin of voids and of changes in void volume as a function of pyrolysis conditions is desired.

2. Experimental procedure

Fibres which were characterized included a standard grade of commercial Si–C–O fibre (Nicalon NLM-101, Nippon Carbon Co., Ltd, Tokyo) containing ~15 wt % O, referred to as SG Nicalon [1, 2]; an

0022-2461/90 $03.00 + .12

Si–C–O ceramic fibre containing ~6 wt % O derived from methylpolysilane polymer, referred to as MPS fibre [6]; and an Si–N–C ceramic fibre derived from hydridopolysilazane polymer, referred to as HPZ fibre [5]. The latter two fibres were developed at Dow Corning under a government-sponsored contract for advanced ceramics based on polymer processing (see Acknowledgements).

Elemental analysis, rule-of-mixtures compositions and gradient-column densities were obtained as previously described [7]. The trace amount of hydrogen found was not included in rule-of-mixtures calculations and trace nitrogen in Si–C–O ceramics was also not included. In MPS fibre the chlorine and aluminium contents, even though appreciable, were also not included. Densities ($g\,cm^{-3}$) used for theoretical-density calculations were: $SiO_2(l)$, 2.20; $Si_3N_4(l)$, 3.0; SiC(l), 3.0; β-SiC, 3.2; C(py), 2.2; porosity, 0 [7].

Weight percentage crystallinity was determined from wide-angle X-ray scattering (WAXS) data by a complete integrated profile analysis corrected for instrumental background [11]. An average crystallite size of β-SiC was measured by line broadening of the (1 1 1) reflection with correction for instrumental broadening [7]. BET (N_2 and krypton) surface areas and mercury porosimetry surface areas as well as pore-size analysis by mercury porosimetry were measured by standard methods [8] and equipment (Quantachrome Corp., Syosset, New York).

Small-angle X-ray scattering (SAXS) patterns over a range of 0.1 to 8° 2θ were obtained using a standard Kratky camera with an 80 μm entrance slit, a 200 μm counter slit and a sample-to-counter distance of 210 mm, operated in a step-scanning mode. Nickel-filtered Cu$K\alpha$ radiation from Philips generator operated at 40 kV and 40 mA was used (λ = 0.15418 nm). The intensity of scattered X-rays was measured with a proportional counter and a pulse height analyser. Pulses were accumulated at each point for 100 sec and the angular increment between steps was preprogrammed.

Background and reference intensities were obtained for each sample in order to obtain the intrinsic intensity of the X-rays scattered by the sample. Scattering intensity from a standard polyethylene sample at 15 nm (0.3° 2θ) was used as a reference to determine the absolute beam intensity.

Powdered samples were ground in a B_4C mortar and pestle. To contain the powder samples, a holder was constructed around a brass shim (0.38 mm thickness), cut to fit into a liquid sample holder and slotted to provide a cavity. Thin films of Mylar provided support for the powder as well as windows for the cell. The windows were discarded after each use to prevent contamination of one sample with another. Because of the nature of the powders, the efficiency of packing in the cell (and hence the mass of sample in the X-ray beam) varied to some extent from sample to sample.

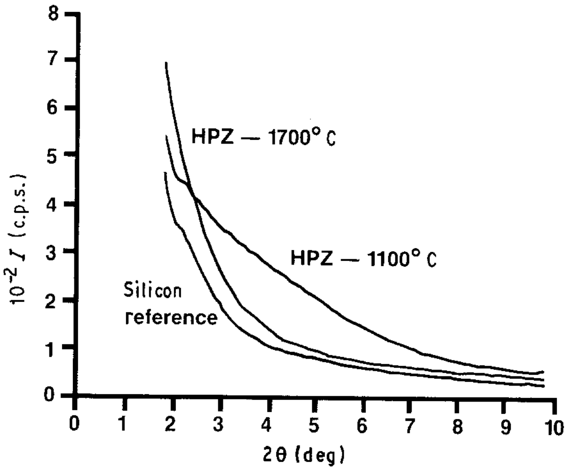

Figure 1 WAXS profiles for fibres 2 and 6.

WAXS patterns from 2 to 10° 2θ were obtained using a Philips generator operated under the same conditions as above. A curved graphite crystal monochromator was used and the scattered radiation was detected using a proportional counter and pulse height analyser. Scattering intensities were corrected by subtracting the scattering of a fully dense, crystalline silicon reference (Fig. 1).

HPZ and a Nicalon sample used to measure fibre orientation were in the form of long fibre bundles which were cut into shorter lengths. The unexposed ends of a bundle were glued to a standard holder so as to be parallel with the long axis of the X-ray beam: the scanning direction was then normal to the axis of the bundle. The fibre bundles were also examined in Gandolfi and Statton cameras with the fibre axes perpendicular to the X-ray beam.

3. Results

3.1. Composition, density and pore fraction

Table I shows pyrolysis temperature and gradient-column densities for six HPZ fibres used. Table II shows similar data, including percentage crystallinity

TABLE I Properties of HPZ ceramic fibres

Fibre	Pyrolysis T (°C)	Fibre diameter (μm)	ρ ($g\,cm^{-3}$)*	Elemental analysis (wt %)†				
				Si	C	N	O	H
1	1000	23.2	2.210	58.1	10.3	27.1	3.01	0.24
2	1100	11.5	2.336	57.0	9.85	28.4	2.70	0.07
3	1200	19.8	2.395	58.1	10.3	27.5	3.01	0.12
4	1300	18.4	2.477	58.6	10.2	28.2	(3.3)	0.03
5	1400	18.8	2.524	59.5	10.4	28.8	(2.67)	0.03
6	1700‡	11.1	2.78 ± 0.05	57.0	9.55	29.1	2.30	(0)

*Gradient-column density.

†( ) Indicates estimated value; Cl < 0.2 in all cases.

‡Fibre 2 was heated in N_2 at 5 MPa pressure to achieve densification without thermal decomposition.

TABLE II Properties of Si–C–O ceramic fibres

Fibre	Sample	Pyrolysis T (°C)	Fibre diameter (μm)	ρ (g cm^{-3})	Elemental analysis (wt %)						
					Si	C	N	O	Other	Crystallite size (nm)	Crystallinity (wt %)
7	SG Nicalon	1100	15.9	2.211	55.4	29.4	0.1	15.0	H, <0.1	0.8	29
8	SG Nicalon	1400	15.3	2.521	55.4	27.7	0.1	14.8	H, <0.1	1.4	41
9	MPS	1200	~15	2.624	59.1	29.3	0.09	6.28	H, <0.1; Cl, 3.41; Al, 0.5	2.0	50

and crystallite sizes, for the Si–C–O fibres used. HPZ fibres were cured on the spinning line [5] and pyrolysed in N_2 at ~3° C min^{-1} to the indicated temperature and then ballistically cooled. Table III shows calculated volume fractions of each phase including pore (void) fraction, P, obtained using the equation

$$P = 1 - (\varrho/\varrho_t) \qquad (2)$$

where ϱ = density measured in a gradient column [7].

3.2. Porosity and surface area

HPZ ceramic fibre pyrolysed to 1100° C (fibre 2) was characterized by mercury porosimetry, which found no pores smaller than ~ 5 μm [8]. This pore-size range corresponds to the void volume between fibres rather than pores within fibres. Surface area by mercury porosimetry for these 11.5 μm diameter fibres was found to be 0.16 m^2 g^{-1}, which corresponds closely to the calculated geometrical surface area of 0.15 m^2 g^{-1}. BET surface area using nitrogen (molecular diameter 0.45 nm) was too small to measure so krypton, a heavier gas (atomic diameter 0.51 nm), was used. Surface area measured was 0.36 m^2 g^{-1}. The increase over geometric surface area may be due to surface roughness. It is certainly not large enough to imply a significant amount of surface-connected porosity. Similar porosimetry and surface area results were found for various samples of Standard Grade Nicalon™ ceramic fibres.

3.3. X-ray diffraction

Fibre samples 2 and 7, as well as other Nicalon and HPZ fibres, were shown to be non-oriented by wide-angle X-ray measurements. Thus, symmetric amorphous haloes with no equatorial enhancement were obtained for HPZ fibre bundles using Statton (flat plate) or Gandolfi (semi-cylindrical plate) cameras [12]. Symmetric circular patterns were also obtained with Nicalon fibre bundles for which the diffracted β-SiC peaks are superimposed on the halo pattern.

3.4. X-Ray scattering

The methods used are described elsewhere [9, 10]. Fig. 2 shows that fibre 2 and presumably the other ceramic fibres are three-dimensional (not of fractal dimension) materials which follow the Porod law over characteristic dimensions of > 2.5 nm [13]. Data obtained using the wide-angle camera (WAXS) were reduced to a set of intensity values as a function of S (see Equation 3 below), corrected for instrumental and background scattering effects by subtracting the scattering intensity of a fully dense, polycrystalline silicon specimen:

$$S = 4\pi \sin\theta/\lambda \qquad (3)$$

Data were treated according to the Guinier approximation (Equation 4) at the low-angle scattering limit (low values of S):

$$\ln \tilde{I}(S) \cong \ln \tilde{I}(0) - \tfrac{1}{3}S^2R_g^2 \qquad (4)$$

where $\tilde{I}(S)$ = background corrected scattering intensity, $\tilde{I}(0)$ = scattering intensity intercept at low angle (0° 2θ) and R_g = average electronic radius of gyration of the scatterer (scattering phase). A plot of $\log \tilde{I}(S)$ against S^2 yields R_g for the scatterer phase.

For a spherical scatterer of radius R_s, R_g can be converted to a spherical equivalent:

$$R_s = R_g(5/3)^{1/2} \qquad (5)$$

An example of a Guinier plot using small-angle equipment (SAXS) is shown in Fig. 3. Data showing R_g and R_s obtained from such Guinier plots are given in Table IV.

Scattering data at the high-angle limit (larger values of S) were analyzed by the Porod law

$$O_s = \left(\frac{8\pi V_2}{a\lambda}\right)\left(\frac{\lim\,[m^3\tilde{I}(m)]}{\tilde{Q}_m}\right) \qquad (6)$$

where $m = 2a\sin\theta$ = linear distance between incident and scattered X-rays in the plane at registration

TABLE III Calculated density and volume fraction of each rule-of-mixtures phase

Fibre	ρ_t*	SiO$_2$(l)	Si$_3$N$_4$(l)	SiC(l)	β-SiC	pyC†	Pore fraction
1	2.916	0.058	0.502	0.157	0	0.041	0.242
2	2.915	0.055	0.560	0.135	0	0.052	0.199
3	2.914	0.062	0.550	0.162	0	0.047	0.178
4	2.907	0.070	0.575	0.156	0	0.051	0.148
5	2.921	0.057	0.593	0.164	0	0.051	0.136
6	2.923	0.056	0.682	0.152	0	0.061	0.049
7	2.659	0.284	0	0.232	0.202	0.114	0.168
8	2.686	0.325	0	0.175	0.326	0.112	0.062
9	2.879	0.149	0	0.251	0.431	0.080	0.089

*Theoretical density calculated from Equation 1.

† Pyrolytic carbon.

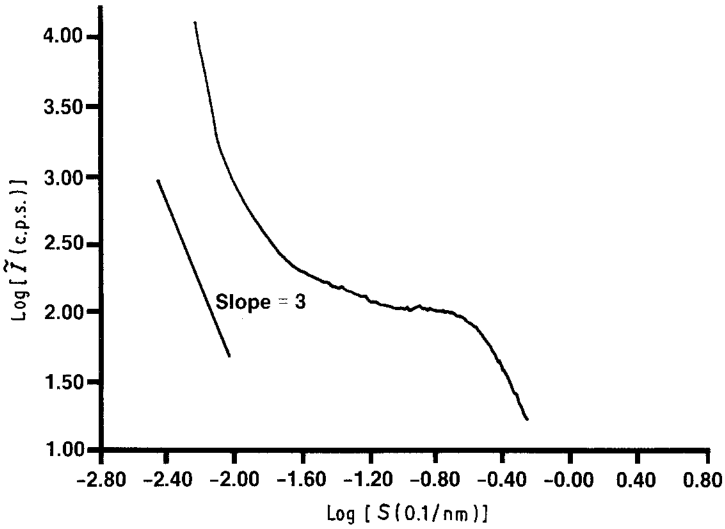

Figure 2 Porod profile for fibre 2.

(a is the distance from sample to X-ray detector); O_s = internal surface area of scatterer per unit scatterer volume; V_2 = volume fraction scatterer phase; $\tilde{Q}_m$ = invariant = $\int_0^\infty m\tilde{I}(m)\,\mathrm{d}m$, using infinite slit geometry; and $\tilde{I}(m)$ = absolute scattering intensity using infinite slit geometry, relative to the primary X-ray beam (obtained from the polyethylene working standard).

$\lim\,[m^3\tilde{I}(m)] = K$ is the asymptote at high scattering angle in a Porod law plot of $m^3\tilde{I}(m)$ against m^3 or the equivalent in S-space as in Fig. 4, using $m = S(a\lambda/2\pi)$. Evaluation of the invariant, $\tilde{Q}_m$, for each material was obtained from a plot of $\tilde{I}(m)$ against m.

Scattering power, $\overline{(\varrho - \bar{\varrho})^2}$, is given by Equations 7 and 8:

$$\overline{(\varrho - \bar{\varrho})^2} = V_1 V_2(\varrho_1 - \varrho_2)^2 \qquad (7)$$

where V_1 = volume fraction of continuous phase and V_2 = volume fraction pore (void) phase ($V_1 + V_2 = 1$); ϱ_1, ϱ_2 = electron density (electrons per unit volume) of each region, and $\bar{\varrho}$ = average electron density. Also

$$\overline{(\varrho - \bar{\varrho})^2} = \left(\frac{2\pi}{i_e N^2}\right)\left(\frac{\tilde{Q}_m}{da\lambda^3}\right) \qquad (8)$$

where i_e = Thompson scattering constant for a free electron (7.9×10^{-26}), N = Avogadro's number, λ = X-ray wavelength (0.154 18 nm) and d = sample thickness.

4. Discussion

Scattering power calculations were used to confirm that scattering is due to porosity and not to other electron density inhomogeneities which are present in these ceramic fibres, such as nanoparticles of elemental carbon or β-SiC [7]. This is shown by Fig. 5, in which scattering power calculated from Equations 7 and 8 is plotted against calculated pore fraction from Table III. Both plots are linear and pass close to the origin as expected if porosity is the only significant scattering phase. The constant ratio (~0.34) between the scattering powers from Equations 7 and 8 is explained by a powder packing fraction of ~0.34 in the Mylar sample cell. This factor arises because the thickness of the cell rather than the true effective thickness of powdered sample in the cell, d, was used in Equation 8. In addition, SG Nicalon fibre 7, with a higher calculated porosity, displays more scattering than SG Nicalon fibre 8 even though fibre 8 contains a larger volume fraction of β-SiC nanocrystallites than fibre 7. This confirms, as expected from the electron density differences ($\varrho_1 - \varrho_2$), that porosity is the only significant scattering phase present in these ceramic fibres.

The equivalent spherical radii of porosity, R_s, obtained from Guinier (Equation 4) and Porod (Equation 6) treatments of the data are similar (Table IV). This similarity indicates that porosity, though not truly spherical, is at least globular in nature.

In the higher pore-fraction samples, the nanoscale porosity is quite extensive as can be seen from a rather simple model illustrating a single two-dimensional layer of randomly spaced pores (Fig. 6). First note that the average pore diameter and the bond length of an Si–N (or Si–C) chemical bond are within an order of magnitude. It is obvious that the pores cannot be truly spherical due to the tetrahedral coordination of silicon oxycarbonitride [Si(N,C,O)$_4$] at the pore interface. A rough pore surface would lead to a smaller R_s from the Porod treatment, based on internal surface

TABLE IV Porosity parameters from X-ray scattering data

Fibre	Guinier $R_g(R_s)$*	Method	Porod $O_s(R_s)$†
1	‡	SAXS	6.28 (0.478)
2	0.585(0.756)	SAXS	6.34 (0.473)
	0.43(0.55)	WAXS§	–
	0.49(0.63)	WAXS§	–
3	0.60(0.77)	SAXS	5.48 (0.547)
4	0.82(1.06)	SAXS	4.23 (0.709)
5	‡	SAXS	2.93 (1.02)
6	1.55(2.0)	SAXS	2.36 (1.27)
7	0.33(0.43)	WAXS	–
8	0.58(0.75)	WAXS	–
9	0.782(1.01)	WAXS	–

*R_g = radius of gyration of porosity (nm), R_s = radius of spherical equivalent from Equation 5 (nm).

†O_s = internal surface area of pores per unit volume porosity (nm^2 nm^{-3} or nm^{-1}), R_s = spherical equivalent (nm) ($R_s = 3/O_s$); all Porod measurements using SAXS.

‡Non-linear Guinier plots.

§Independent measurements on different portions of the same sample.

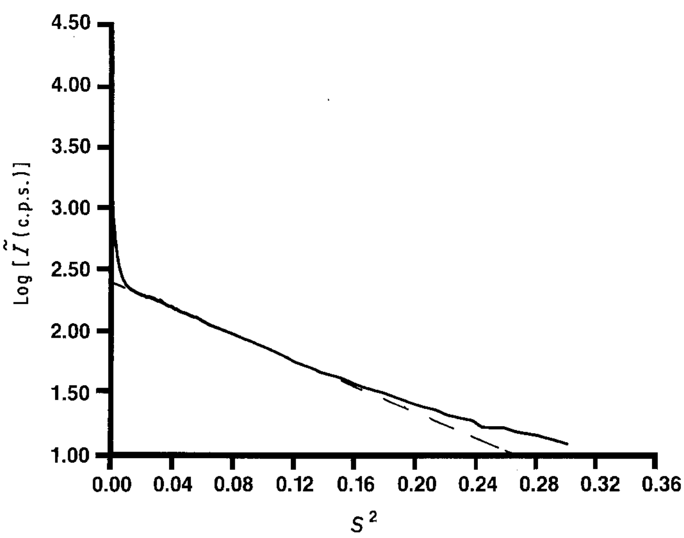

Figure 3 Guinier plot for fibre 3; SAXS data.

area, than from the Guinier treatment, based on a volume average $\tilde{R}_g$, as is found. Note that the specific surface area of the pore interface, O_s, which must consist of high-energy distorted chemical bonds, and perhaps dangling bonds, is very large in samples pyrolysed at low temperature (Table V). In thermodynamic terms, the surface free energy of such a structure is large. Thus surface area will tend to decrease with increasing pyrolysis temperature. As shown by the data, this results in an increase in average pore diameter with increasing pyrolysis temperature but a decrease in pore fraction and an increase in density. In macroscopic terms, this reduction in pore volume (densification) is seen as a pronounced shrinkage in length of polymer-derived ceramic fibres as they are heated above their pyrolysis temperature [14]*. Heating below the pyrolysis temperature results in a normal increase in length due to thermal expansion.

In the classical X-ray scattering treatment, the positions of the scatterer species are truly random (uncorrelated) because they are dilute, and the scattering curves show no maxima. In these ceramic fibres, especially those of higher porosity, it is apparent that the distances between pores cannot be random because of constraints imposed by the ratio of pore diameter ($2R_s$) to average distance between pores ($\bar{l}$) approaching unity rather than zero as in the dilute scatterer case. Thus shallow maxima in the scattering curves are observed at an angle approximately corresponding to the average distance between pores ($\bar{l}$) in the classical Bragg reflection equation

$$\bar{l} = d = \lambda/(2\sin\theta) \qquad (9)$$

In terms of the scattering vector S (Equation 3), the scattering maximum is

$$S_{\max} = 2\pi/\bar{l} \qquad (10)$$

The average distance between neighbouring pores, $\bar{l}$, can also be calculated from the porosity or pore fraction, P, in Table III and the spherical radius of porosity, R_s, in Table IV. R_s was obtained from Guinier plots using SAXS data for consistency. The average

TABLE V SAXS data for HPZ fibres

Variable	Fibre					
	1	2	3	4	5	6
Sample thickness (cm)	0.0381	0.01	0.0381	0.0381	0.0381	0.0381
Scattering peak (nm)*	~2.6	–	~3.0	~5.0	–	~14.1
Calculated $\bar{l}$ (nm)†	–	2.1	2.2	3.2	–	8.8
Porod K (c.p.s. cm^3)‡	491.2	305.1	348.9	205.2	125.9	56.1
Area (c.p.s. cm^2)	460.4	298.6	405.9	320.7	287.8	175.2
$\tilde{Q}_m$ (c.p.s.)	23 020	14 930	20 300	16 030	14 390	8764
O_s (nm^{-1})	6.28	6.30	5.48	4.23	2.93	2.36
Scattering power§ (mole-electrons $cm^{-3})^2$	0.1377	0.1288	0.1020	0.0846	–	0.0318
Scattering power¶ (mole-electrons $cm^{-3})^2$	0.3880	0.3771	0.3095	0.2667	–	0.0986
Corrected scattering power[a]	0.405	0.379	0.300	0.249	–	0.0935
Scattering power ratio[b] Eqn 8/ Eqn 7	0.355	0.382	0.330	0.317	–	0.323

*From Equation 10.
†From Equation 12.
‡c.p.s. = counts per second.
§From Equation 8.
¶From Equation 7.
[a] (1/0.34) × scattering power from Equation 8.
[b] Corresponds to apparent powder packing factor, 0.34 average.

---

*This report describes shrinkage of Nicalon fibres. Similar shrinkage is seen for HPZ fibres on heating above their pyrolysis temperature.

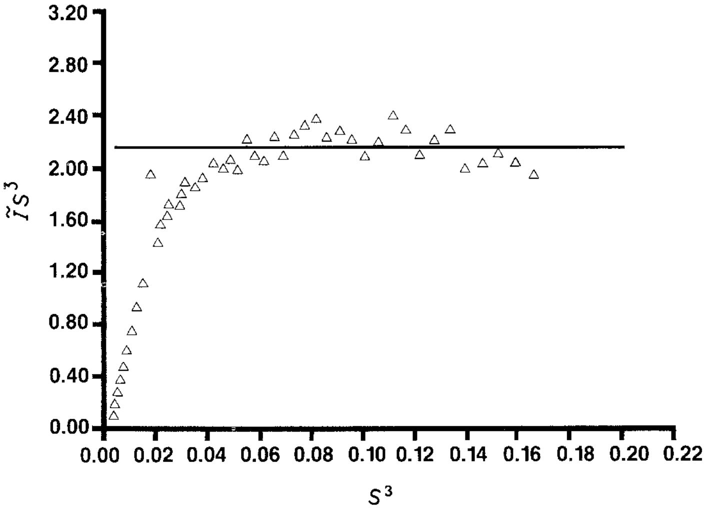

Figure 4 Porod law plot for fibre 2; SAXS data.

number of pores per unit volume of ceramic, n, is

$$n = P/(\tfrac{4}{3}\pi R_s^3) \qquad (11)$$

The average distance between neighbouring pores, $\bar{l}$, is

$$\bar{l} = (1/n)^{1/3} \qquad (12)$$

A rough agreement between $\bar{l}$ calculated from Equations 10 and 12 is shown in Table V.

4.1. Origin of nanoporosity

During pyrolysis of the cross-linked polymeric fibres used to prepare the ceramic fibres, the rate of gas evolution reaches a maximum at ~400 to 600° C at typical heating rates of several degrees per minute [2, 5, 6]. Gas evolution continues to ~900° C and the ceramic fibre reaches a density of $\sim 2\,\mathrm{g\,cm^{-3}}$. Assuming a typical polymer density of $1.1\,\mathrm{g\,cm^{-3}}$ and 70% mass retention, a volume shrinkage of 62% occurs. As the polymer crosslinks and densifies, the evolution of pyrolysis gases occurs throughout a material which is becoming more resistant to the diffusion of pyrolysis gases as it converts from a polymer to a ceramic solid. It can be estimated from the gas law that hundreds of volumes of gases are evolved per volume of polymer fibre pyrolysed [7]. The rate of gas evolution at a typical heating rate of $3°\mathrm{C\,min^{-1}}$ is far too high for diffusion through the solid phase to be an important route for gas loss. Only in thin fibres or films does conversion to ceramic occur without macroscopic foaming.

It is likely that a network of nanochannels forms in the fibres to permit the escape of pyrolysis gases without macroscale foam formation, in contrast to the foaming seen in pyrolysis of bulk polymer samples. Thus, in the HPZ system it has been found that the partially pyrolysed polymer fibres formed at 400 to 800° C are highly reactive towards air and moisture when first removed from a pyrolysis furnace [15]. A rapid exothermic reaction occurs initially without evolution of NH_3, which may involve oxidation of unsaturated bonds. A slower hydrolysis reaction with evolution of NH_3 and incorporation of hydrogen in the partially pyrolysed fibre occurs over several days. Large quantities of oxygen are incorporated in the fibre by these reactions and the weight gain approaches 30%. These results are consistent with a high surface area fibre. For example, after air exposure and the resulting oxidation and hydrolysis, fibres pyrolysed to 600° C gave a BET (N_2) surface area of $8.2\,\mathrm{m^2\,g^{-1}}$ compared to the very small BET surface area described above for a fibre pyrolysed at 1100° C. Measurements of the highly reactive product before air and moisture exposure would be likely to give much higher specific surface areas because amorphous silica produced on oxidation or hydrolysis of Si_3N_4 will close surface-connected pores. This can be seen from the volume equivalent of the relevant species in $\mathrm{cm^3}$ per silicon equivalent: $SiN_{4/3}$, 15.6; SiC, 13.3; SiO_2, 27.3. Thus formation of amorphous (or crystalline) silica on the surface of an Si_3N_4-like or SiC-like

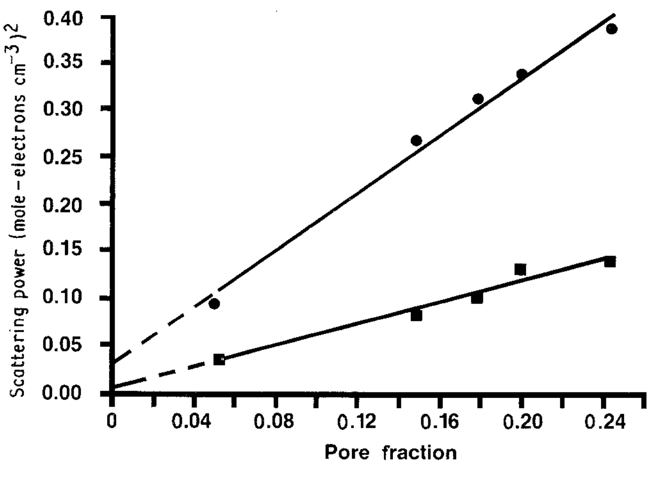

Figure 5 Scattering power against calculated pore fraction: (●) Equation 7, (■) Equation 8.

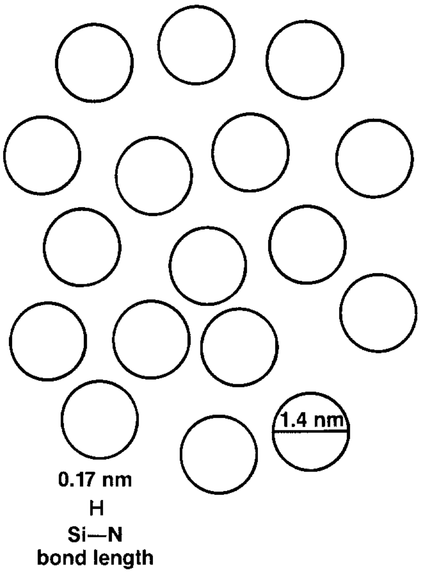

Figure 6 Two-dimensional representation of porosity in fibre 2 ($P = 0.2$).

ceramic fibre leads to considerable volume expansion which would tend to close surface-connected porosity.

Fibres become insensitive to air and moisture if pyrolysed to a temperature (≧900° C) above that to which gas evolution occurs. It is assumed that cylindrical nanochannels collapse to a series of closed nanopores of larger diameter, thus reducing surface area and free energy as has been shown for viscous systems [16]. Increasing temperature would permit viscous flow to occur, which is the most likely mechanism by which such a collapse could occur. On further heating, nanopores increase in average diameter and the volume fraction of pores decreases. Again, a decrease in surface free energy drives this densification process. Similar phenomena have been reported in the transformation of highly porous silica gels to glass in the sol–gel–glass process [17–19].

The Young's moduli of Nicalon [2] and HPZ [15] ceramic fibres increase with increasing density and pyrolysis temperature up to the point at which thermal degradation occurs. Increasing modulus is expected as pore fraction decreases.

5. Conclusions

X-ray scattering measurements showed that porosity present in ceramic fibres derived from polymer precursors is due to globular nanopores. Pore fractions range from 0.05 to 0.25. The nanopores increase in average size but decrease in volume fraction as the pyrolysis temperature is increased. This thermodynamically favourable decrease in surface area appears to occur by a viscous flow process.

Nanochannels are apparently formed during the early stages of the pyrolysis process during loss of large volumes of pyrolysis gases. Nanopores are formed in the latter stages of the pyrolysis process by viscous collapse of nanochannels accompanying ceramic densification. Densification and decrease in pore volume leads to increased elastic modulus of ceramic fibres.

Acknowledgements

This work was performed under Air Force Contract F33615-83-C-5006 sponsored by the Material Sciences Division of the Defense Advanced Research Projects Agency and administered by Air Force Systems Command, Aeronautical Systems Division/PMRRA, Wright-Patterson AFB, Ohio. We thank the programme managers, A. P. Katz and B. Wilcox, for their support and encouragement.

References

1. S. YAJIMA, Y. HASEGAWA, J. HAYASHI and M. IIMURA, *J. Mater. Sci.* **13** (1978) 2569.
2. Y. HASEGAWA, M. IIMURA and S. YAJIMA, *ibid.* **15** (1980) 720.
3. T. MAH, M. G. MENDIRATTA, A. P. KATZ and K. S. MAZDIYASNI, *Amer. Ceram. Soc. Bull.* **66** (1987) 304.
4. *Idem, ibid.* **66** (1987) 317.
5. G. E. LEGROW, T. F. LIM, J. LIPOWITZ and R. S. REAOCH, *ibid.* **66** (1987) 363.
6. J. LIPOWITZ, G. E. LEGROW, T. F. LIM and N. LANGLEY, *Ceram. Eng. Soc. Proc.* **9** (1988) 931.
7. J. LIPOWITZ, H. A. FREEMAN, R. T. CHEN and E. R. PRACK, *Adv. Ceram. Mater.* **2** (1987) 121.
8. S. LOWELL and J. E. SHIELDS, "Powder Surface Area and Porosity," 2nd edn (Chapman and Hall, New York, 1984).
9. O. GLATTER and O. KRATKY (eds), "Small Angle X-ray Scattering" (Academic, New York, 1982).
10. L. E. ALEXANDER, "X-Ray Diffraction Methods in Polymer Science" (Krieger, Huntington, New York, 1979) Ch. 5.
11. L. K. FREVEL and W. C. ROTH, *Anal. Chem.* **54** (1982) 677.
12. L. E. ALEXANDER, "X-Ray Diffraction Methods in Polymer Science" (Krieger, Huntington, New York, 1979) Ch. 2.
13. D. W. SCHAEFER, *Mater. Res. Bull.* **13** (1988) 22.
14. H. S. STARRETT, Report SoRI-EAS-85-620 (Southern Research Institute, Birmingham, Alabama, 1985).
15. J. A. RABE, unpublished data (1986).
16. F. D. RUMSCHEIDT and S. G. MASON, *J. Colloid Sci.* **17** (1962) 260.
17. C. J. BRINKER and G. W. SCHERER, *J. Non-Cryst. Solids* **70** (1985) 301.
18. C. J. BRINKER, G. W. SCHERER and E. P. ROTH, *ibid.* **72** (1985) 345.
19. G. W. SCHERER, C. J. BRINKER and E. P. ROTH, *ibid.* **72** (1985) 369.

Received 13 December 1988
and accepted 23 August 1989